PPPL-3173 - Preprint: May 1996, UC-420, 426

Design and Operation of the Pellet Charge Exchange Diagnostic for Measurement of Energetic Confined Alphas and Tritons on TFTR

S. S. Medley, H. H. Duong†, R. K. Fisher*, N. N. Gorelenkov+, A. V. Khudoleev++, D. K. Mansfield, J. M. McChesney*, P. B. Parks*, M. P. Petrov++, and A. L. Roquemore

Princeton Plasma Physics Laboratory, P. O. Box 451, Princeton, New Jersey 08543 USA

† General Atomics ORAU Fellow

** General Atomics, San Diego, California 92186 USA*

+ TRINITI, Troisk 142092 Russia

++A. F. Ioffe Physical-Technical Institute, St. Petersburg, 194021 Russia

Abstract

Radially-resolved energy and density distributions of the energetic confined alpha particles in D-T experiments on TFTR are being measured by active neutral particle analysis using low-Z impurity pellet injection. When injected into a high temperature plasma, an impurity pellet (e.g. Lithium or Boron) rapidly ablates forming an elongated cloud which is aligned with the magnetic field and moves with the pellet. This ablation cloud provides a dense target with which the alpha particles produced in D-T fusion reactions can charge exchange. A small fraction of the alpha particles incident on the pellet ablation cloud will be converted to helium neutrals whose energy is essentially unchanged by the charge transfer process. By measuring the resultant helium neutrals escaping from the plasma using a mass and energy resolving charge exchange analyzer, this technique offers a direct measurement of the energy distribution of the incident high-energy alpha particles. Other energetic ion species can be detected as well, such as tritons generated in D-D plasmas and H or He^3 RF-driven minority ion tails. The diagnostic technique and its application on TFTR are described in detail.

1. Introduction

The effective operation of a D-T fusion reactor requires that the alpha particles generated in D-T fusion reactions be well confined to allow deposition of most of the alpha energy in the plasma before they are lost. Several diagnostics designed to measure confined alphas in large tokamaks recently began operation in tokamak experiments; namely, charge exchange spectroscopy[1], microwave scattering[2], and energetic neutral particle analysis with the use of low-Z impurity pellets[3,4]. The last method, which we call Pellet Charge Exchange (PCX), was developed in a collaboration between General Atomics, the A. F. Ioffe Physical-Technical Institute and the Princeton Plasma Physics Laboratory and is now operated routinely on TFTR during D-T experiments. PCX diagnostic results have been reported on measurements of RF-driven energetic 3-helium[5], hydrogen[6] and tritium[7] minority ion tails, the energy distribution of fast confined alpha particles and tritons[8-9], and the influence of magnetic field ripple and sawtooth oscillations on the behavior of the alpha energy spectra and radial density distributions[10-12].

In the PCX diagnostic on TFTR, low-Z impurity pellets are injected along a midplane major radius. Upon entering the plasma, the pellet forms a toroidally elongated ablation cloud, as illustrated in Fig. 1. Using lithium pellets as an example, the possible charge changing reactions for alpha particles passing through a slab of Li^+ plasma are:

$$He^{2+} + Li^+ \Rightarrow He^+ + Li^{2+} \quad (1a)$$
$$He^+ + Li^+ \Rightarrow He^0 + Li^{2+} \quad (1b)$$
$$He^{2+} + Li^+ \Rightarrow He^0 + Li^{3+} \quad (1c)$$
$$He^+ + Li^+ \Rightarrow He^{2+} + Li^0 \quad (1d)$$
$$He^+ + Li^+ \Rightarrow He^{2+} + Li^+ + e^- \quad (1e)$$
$$He^+ + e^- \Rightarrow He^{2+} + 2\,e^- \quad (1f)$$
$$He^0 + Li^+ \Rightarrow He^+ + Li^0 \quad (1g)$$
$$He^0 + Li^+ \Rightarrow He^+ + Li^+ + e^- \quad (1h)$$
$$He^0 + e^- \Rightarrow He^+ + 2e^- \quad (1i)$$
$$He^0 + Li^+ \Rightarrow He^{2+} + Li^0 + e^- \quad (1j)$$
$$He^0 + Li^+ \Rightarrow He^{2+} + Li^+ + 2e^-. \quad (1k)$$

A small fraction of the alphas incident on the Li^+ species in the ablation cloud is

neutralized either by sequential single electron capture (Eq. 1a and 1b) or by double electron capture (Eq. 1c). The remaining reactions in the list are of relevance in the detailed computation of the charge composition of alpha particles passing through a Li^+ plasma cloud[13]. Equations analogous to Eqs. (1) can be written to describe the effects of Li^{2+} and Li^{3+}.

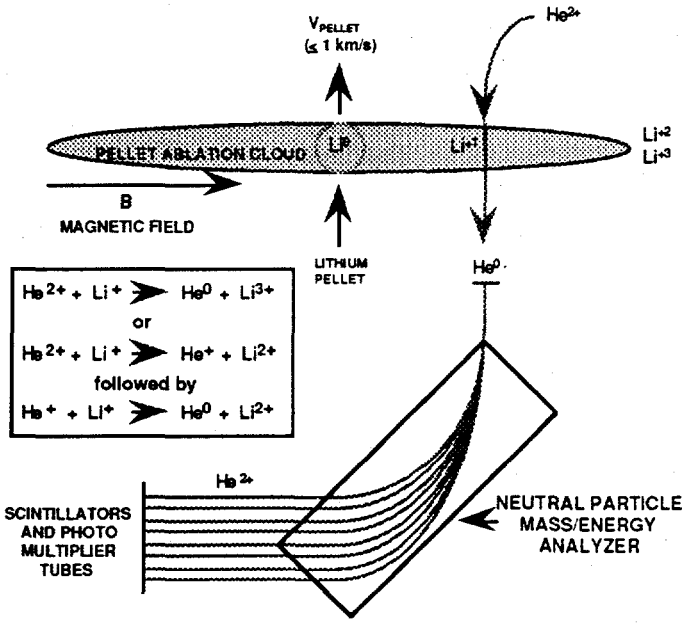

Fig. 1 Illustration of the Pellet Charge Exchange (PCX) technique using lithium pellet injection.

If the line integral target density for particles traversing the cloud is sufficiently large, then the fraction of particles emerging from the cloud as neutrals approaches the equilibrium fraction, $F_0^\infty(E)$, which is independent of the linear density of the cloud. Pitch angle scattering and energy loss are not important at the cloud densities expected in TFTR[13].

By measuring of the energy distribution, dn_0/dE, of the resultant helium neutrals escaping from the pellet ablation cloud, the energy distribution of the incident alpha particles, dn_α/dE, can be determined using $dn_\alpha/dE = (dn_0/dE) \div F_0^\infty(E)$ where $F_0^\infty(E)$ is the neutral equilibrium fraction for helium incident on the cloud.

This paper provides a detailed description of the design, calibration and operation of the Pellet Charge Exchange diagnostic on TFTR.

2. Description of the Pellet Charge Exchange (PCX) Apparatus

The escaping energetic neutrals are mass and energy analyzed using a GEMMA-2 high energy E||B Neutral Particle Analyzer (NPA) that was designed, manufactured and calibrated by the Ioffe Institute[14] with the use of a cyclotron accelerator. Operation of the NPA is based on ionization of the atoms by stripping in a

neutral flux from the tokamak. The foil is located at the entrance to the magnet pole gap and consists of a 400Å thick carbon foil supported on a mesh having 74% transparency. The neutrals enter the stripping foil at an angle of 45^{o}. For D-T operation, three foils are mounted inside the analyzer on a slide mechanism which is manually positioned with a metal welded-bellow linear vacuum actuator. The additional foils are for redundancy in the event of a foil rupture. The secondary ions produced after stripping are deflected through an angle of 90^{o} by the magnetic field. The magnet pole dimensions are 20 cm x 60 cm with a pole gap of 10.5 mm. After passing through the magnet, a parallel, fan-like particle beam with momentum dispersion is formed. This beam passes through the electrostatic condenser which disperses the ions with the same Z/E value by h = 5 cm from the midplane of the instrument to the location of the scintilllator detectors.

The flight tube, collimator and NPA analyzer chamber with a volume of approximately 50 liters are evacuated by a Balzer 510 turbo pump that provides an operating base pressure of $< 2x10^{-7}$ Torr. For reasons of tritium safety compliance, all the NPA seals are metallic (either Conflat or Helicoflex).

The analyzer has eight energy channels, each provided with a scintillator comprised of an ~ 5μ thick layer of ZnS(Ag) which is deposited on 3 cm diameter by 1 mm thick glass substrate and coated with a 0.05μ Al layer for light reflection. When installed on the eight 2.8 cm diameter vacuum windows welded into the detector flange, the scintillators are masked down to provide an effective detection area of 1.0 cm in the mass dispersion direction and 2.0 cm in the energy direction. The ions enter the scintillator at an angle of 20^{o} from the plane of the scintillator so that the effective thickness of the scintillator matches the range of the incident alphas. The scintillator light emission is measured by Hamamatsu H31 67-01 phototubes operated with biases ranging from 0.8 - 1.6 kV. In the PCX setup, the phototube/amplifier electronics are operated primarily in the current mode with a selectable bandwidth up to 5 MHz. Under low signal level conditions, the electronics can effectively be operated in the pulse counting mode as well. Single pulses from the ZnS(Ag) scintillator have a pulse width of ~10 μs.

A block diagram of electronic instrumentation for device control and data acquisition is shown in Fig. 3. The PCX diagnostic is controlled through CICADA, the Central Instrumentation Control and Data Acquisition system for TFTR.

In addition to the neutral particle detectors, the PCX is also equipped to monitor the neutron and gamma-ray induced background at the instrument as well as light emission from the pellet ablation cloud. For neutron and gamma-ray monitoring, a

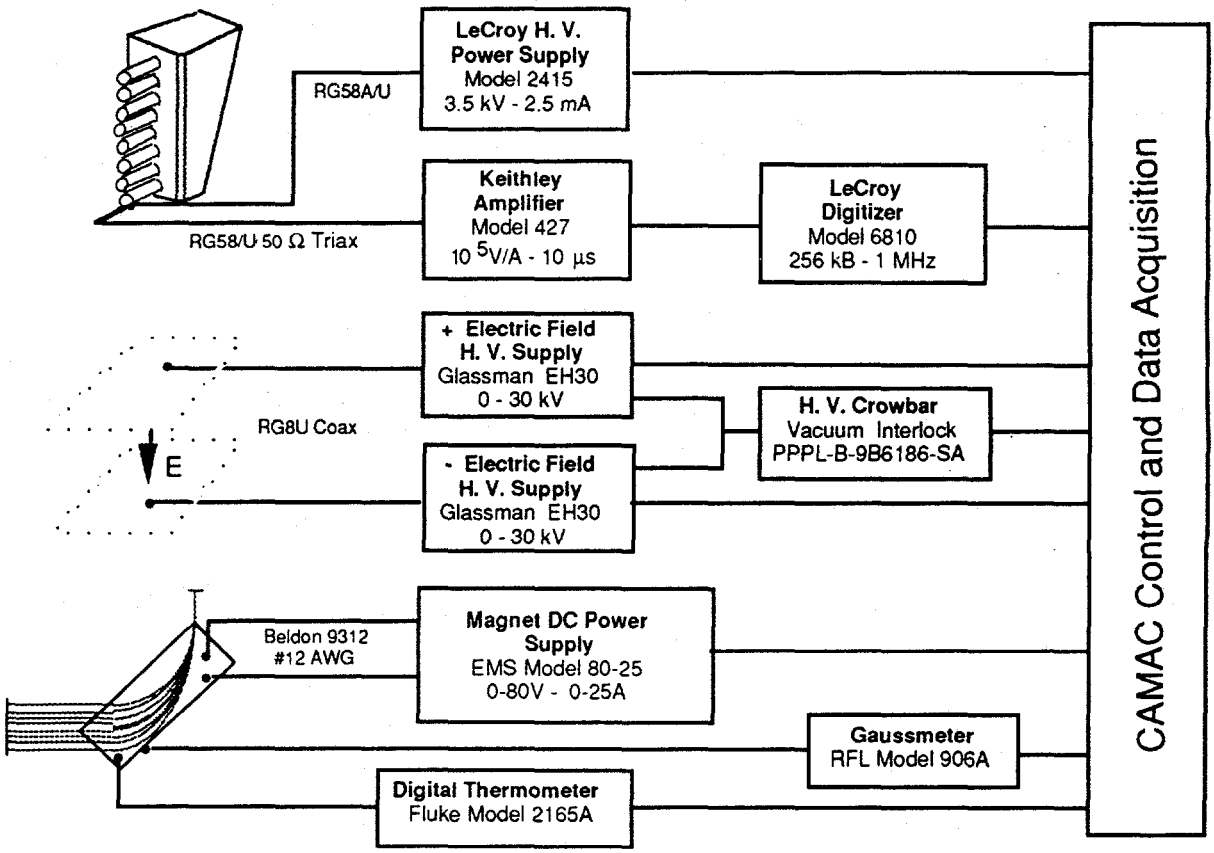

Fig. 3 Block diagram of the electronic instrumentation for the Neutral Particle Analyzer (NPA).

separate magnetically shielded Hamamatsu phototube complete with a scintillator and other elements to replicate the particle detectors is mounted in close proximity to the particle-measuring phototubes. This signal is useful, for example, to confirm that the phototubes remain in a linear operating regime even in the presence of large neutron background signal levels. The NPA is equipped with a straight through port which enables viewing down the PCX flight tube to monitor light emission from the pellet ablation cloud with the same field of view as the NPA. A fiber optic bundle installed at this port relays the pellet light to phototubes located outside the TFTR test cell. The fiber output is split into three separate channels which are provided with line filters for the 6708Å Li^0, 5485 Å Li^+, and 4499Å Li^{++} emission lines with the goal of monitoring the ionization state mix of the ablation cloud. All filters have a ±50Å FWHM bandpass. Typical pellet cloud light signals imply that Li^0, Li^+ and Li^{++} are present in the region of the cloud viewed by the NPA. At the 4499Å wavelength, however, it is not clear whether the observed signal is due to Li^{++} line radiation or cloud continuum radiation. The light emission also serves to check the quality of the injected pellet; for example, whether or not the pellet fragmented or was deflected out of the NPA field of

view during injection.

The interior of the collimator, straight through port and detector chamber were painted with a black, conductive carbon pigment paint (Micro-Circuits Co. Type RS17) in order to suppress pickup on the phototubes of light from the pellet ablation cloud. Data taken with the analyzer deflection fields turned off confirm that the light pickup is negligible.

The Impurity Pellet Injector (IPI) that was used in conjunction with the PCX diagnostic was built by MIT and is capable of injecting Li, B and C pellets using either hydrogen or helium as the gas propellant. A schematic of the PCX field-of-view relative to the IPI pellet trajectory is shown in Fig. 4. The IPI axis lies on a major radius of TFTR and the PCX axis makes a selectable oblique angle of 2.75°, 13°, or 18.37° with the IPI axis, to allow viewing of the cloud at different toroidal distances from the pellet. In the present configuration, the analyzer views the pellet from behind with a sight line at a toroidal angle of 2.75° to the pellet trajectory. Consequently, onlynear perpendicular alphas with velocities close to $V_{||}/V = -0.048$ are detected by the diagnostic. The pellet velocity and its radial position as a function of time is measured using a linear photodiode array situated on the top of the vacuum vessel. This fan-like array consists of 12 chords which intersect the pellet trajectory at 10 cm intervals in the plasma midplane. By combining this measurement with the time dependence of the observed helium neutral signal, radially resolved alpha energy spectra and alpha density radial profiles can be derived with a radial resolution of ~ 5 cm.

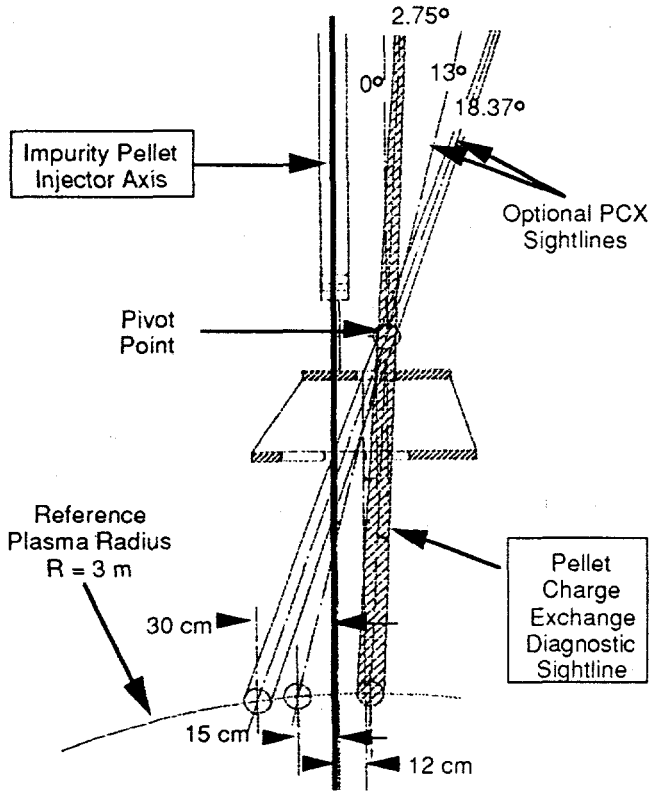

Fig. 4 Field-of-view of the Pellet Charge Exchange (PCX) diagnostic relative to the pellet flight path of the Impurity Pellet Injector.IPI). The PCX apparatus is currently installed at the 2.75° position.

Neutron and gamma-ray induced background is very serious problem for many diagnostics in D-T experiments. Although the scintillator detectors are relatively insensitive to neutrons and gammas, for D-T operations on TFTR it was necessary to install radiation shielding around the NPA. This radiation shield consists of four inches of lead inside six inches of borated polyethylene, as illustrated in Fig. 5. In order to determine the effectiveness of the shield, a detector assembly identical to the NPA detectors was mounted immediately outside the shield and the ratio of the neutron-induced signals between the outside and inside detectors was measured. As seen in Fig. 6, the shielding factor for a D-D discharge which is dominated by 2.5 MeV

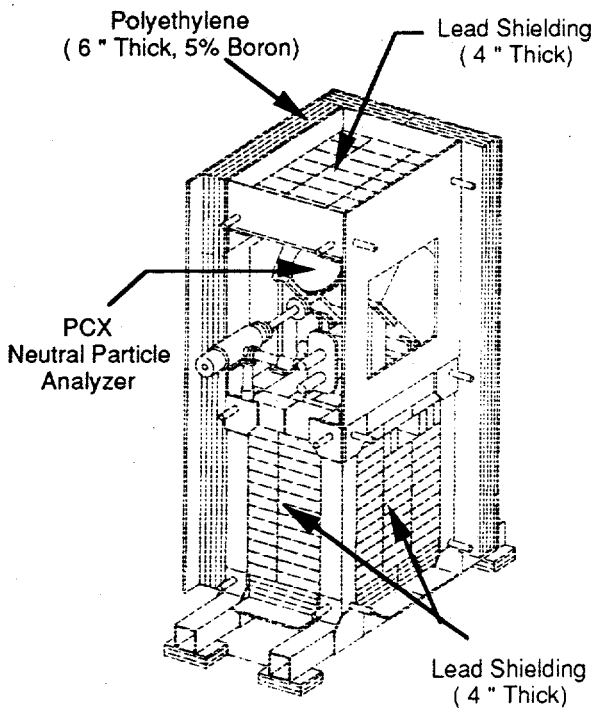

Fig. 5 Schematic of the neutron and gamma radiation shield installed around the NPA for D-T operation on TFTR.

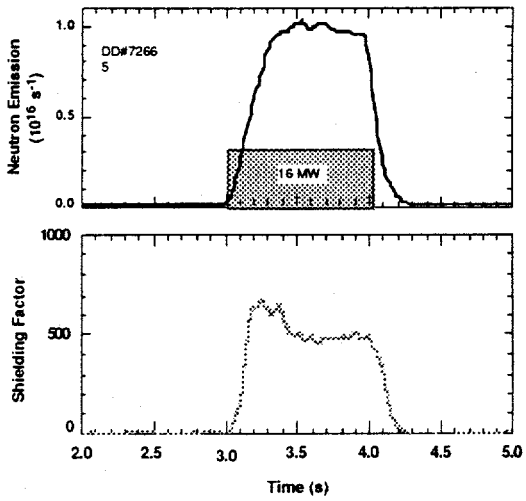

Fig. 6 For a D-D plasma, the measured shielding factor is ~ 500.

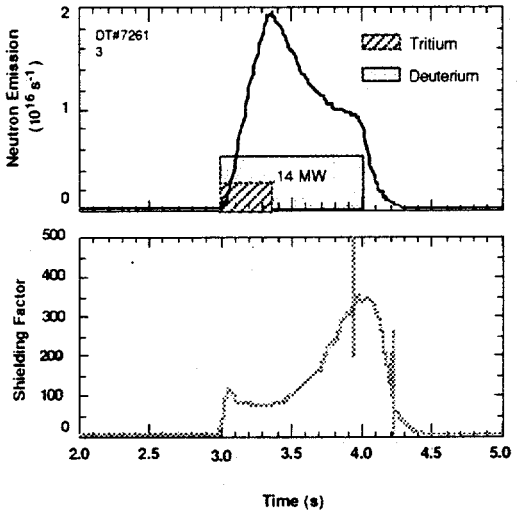

Fig. 7 For a D-T plasma, the measured shielding factor is ~ 100

neutrons is ~ 500. In Fig. 7, both deuterium and tritium neutral beams were injected into a deuterium plasma with the tritium injection terminated after ~ 0.35 s. During the initial phase of beam heating when the 14 MeV neutron yield is dominant, the shielding factor is ~ 100 which subsequently climbs toward the value for 2.5 MeV neutrons as the 14 MeV component decays after termination of tritium beam injection. Thus, the measured shielding factor for neutron and gamma background radiation is taken to be ~ 100 for D-T plasmas and ~ 500 for D-D plasmas.

3. Calibration of the PCX Diagnostic

The NPA was calibrated at the Ioffe Institute with a cyclotron accelerator which produces beams of protons and helium ions that were converted into neutral beams of hydrogen and helium atoms having known absolute intensity and energy in the energy range of 0.2 - 4 MeV. The NPA parameters that were determined during this calibration process are described below.

3.1 Basic NPA Operating Specifications.

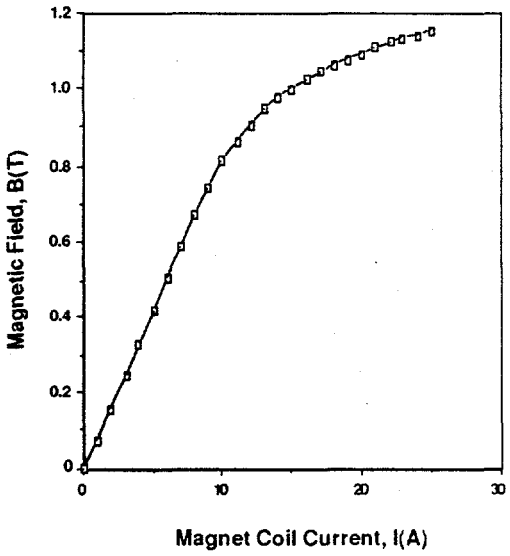

Fig. 8 Magnetic field calibration of the Neutral Particle Analyzer.

3.1.1 Energy calibration

The relationship between the magnetic field, B(T), and analyzing voltage, U_C(kV), for detection of a given ion species is expressed in terms the energy of the highest channel, E_8, by

$$B(T) = 0.54\,[A\,E_8\,(MeV)]^{1/2} / Z \quad (2)$$

$$U_C(kV) = \pm\, 10.8\,E_8\,(MeV)\,/Z \quad (3)$$

where A, Z are the mass and charge of the detected particles, respectively. In practice, the maximum allowable condenser voltage of ± 20 kV limits the maximum accessible energy to ≤ 3.7 MeV for He^{++} and ≤ 1.85 MeV for H^+. Fig. 8 shows the measured magnetic field as a function

of coil current for the NPA coils connected in series. For magneti coil currents in the range of I(A) = 0 - 25 amperes, the relationship between the magnetic field, B(T), and the current, I(A), can be represented by:

$$B(T) = 2.000 + 6.084 \times 10^{-1}\, I(A) + 9.075 \times 10^{-2}\, I(A)^2 - 1.057 \times 10^{-2}\, I(A)^3 + 3.952 \times 10^{-4}\, I(A)^4 - 5.089 \times 10^{-6}\, I(A)^5. \quad (4)$$

3.1.2 Energy range

The analyzer is capable of measuring alphas with energies up to 3.7 MeV. The ratio of the energy detected in the nth channel, E_n, to the highest energy channel, E_8, is shown in Table I. The ratio of the maximum-to-minimum energy measured by the NPA for any magnetic field setting is $E_8/E_1 = 3.76$.

3.1.3 Energy resolution, $\Delta E_n/E_n$

The energy resolution, $\Delta E_n/E_n$, varies from 11.3% to 5.8% as shown in Table I for channels n = 1 - 8 where ΔE_n and E_n are the energy width and average energy, respectively, of the nth channel. It follows from Eq. (2) that the energy resolution varies as $\Delta E_n/E_n \propto E^{-1/2}$.

Table I
NPA Calibration Data

Nch	1	2	3	4	5	6	7	8
E_n/E_8	0.245	0318	0.404	0.498	0.608	0.727	0.857	1.0
$\Delta E_n/E_n$, %	11.3	9.4	8.5	7.4	6.7	6.1	5.8	5.6

3.1.4 Detection efficiency, $\eta_{He,H(E)}$, for He^o and H^o atoms.

The values of the detection effeciency for helium neutrals, η_{He}, constructed from individual channel data versus the energy of alphas for the range 0.3 - 3.7 MeV are shown in Fig. 9. Due to scattering in the stripping foil, limited transparency of the supporting mesh and defocusing effect of the edge magnetic field, measured

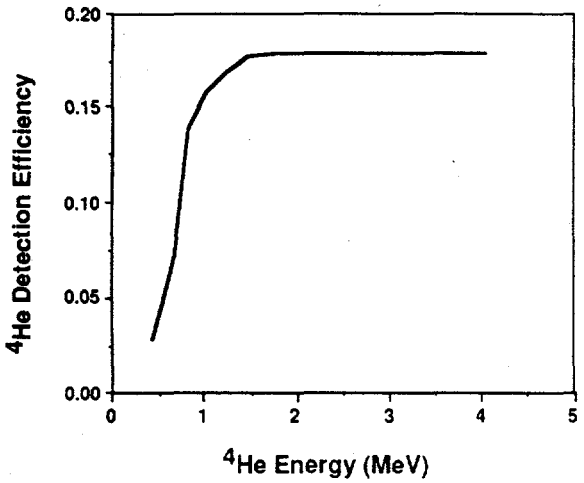

Fig. 9 NPA alpha particle detection efficiency as a function of alpha energy. This efficiency accounts for neutral ionization in the stripping foil and ion optics in the analyzer magnetic and electric fields.

efficiencies are a few times smaller than can be expected from the equilibrium fractions in a carbon foil. For hydrogen atoms, the values of η_H are constant in this energy range and equal to 0.18.

3.1.5 Mass Resolution

The mass resolution of the NPA depends on the width of the collimator slit and the active scintillator width in the mass dispersion direction; i.e. the direction of the condenser electric field. For all experimental scenarios of interest on TFTR, only very coarse mass resolution is required because of the absence of any significant density of unwanted ion species in the MeV energy range that could contaminate the desired measurement. For example, during D-T discharges the triton density from D-D reactions is almost two orders of magnitude less than the alpha density so contamination of the alpha particle measurements by tritons is not a problem. In fact, mass resolution for alpha particle measurements is required only because of the production of unwanted He^+ along with He^{++} during reionization of the neutral alphas in the stripping foil. For a given detector channel of the NPA, the mass dispersion scales as $h \propto Z/E$. Using Eq. (2), the displacement ratio for these ion species is $h_{He^+}/h_{He^{++}} = 2$ or the displacement of He^+ is twice that for He^{++}. Thus, when an NPA channel is tuned for He^{++} at energy E with the correct mass displacement of $h_{He^{++}} = 5$ cm, for the same channel the He^+ component at energy 0.25E will be displaced by $h_{He^+} = 10$ cm. Even with the estimated coarse mass resolution of $\Delta M/M \sim 25\%$ for the NPA configuration on TFTR, separation of the He^+ component from the He^{++} species is satisfactory.

3.2. Normalization of the NPA Channels using Plasma Signals.

In multichannel systems, it is very important to periodically check the relative sensitivity of the channels. For this purpose, we use the counting mode to observe individual H neutral pulses resulting from RF-driven H^+ minority ion tails in TFTR. This signal, which was first observed on JET[15], is produced as a result of neutralization of H^+ RF-driven minority ions by hydrogen-like impurity ions (mainly C^{+5} in TFTR). In TFTR, an H^+ minority signal with a counting rate of a few kHz in the MeV range is detected routinely by the NPA for H^+ minority RF heating at $P_{RF} > 1$- 2 MW. Under these conditions, the neutron and gamma-ray induced background is small.

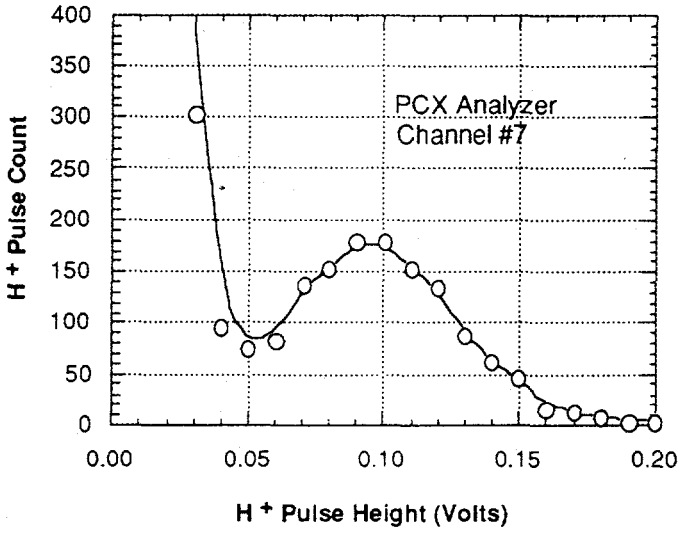

Fig. 10. Example of the H^+ pulse height distribution for NPA Channel #7 obtained by measuring the RF-driven minority hydrogen tail .

The procedure for channel-to-channel normalization is as follows. The H^+ minority signal is obtained during a TFTR discharge in the range of 0.266 - 1.0 MeV in all eight NPA channels with all channels having the same phototube bias. With the use of pulse height analysis, the pulse height spectrum of H^+ pulses for each channel is obtained. An example of such a spectrum for the 7th NPA channel is presented in Fig. 10, where the energy of the detected H^+ ions is 0.855 MeV and the phototube bias voltage is 1.2 kV. The average pulse height for the channel is determined from this spectrum. The average pulse height, normalized to the energy of H^+ ions for each of

the eight NPA channels, is given by the open circles in Fig. 11. Over all channels, the sensitivity is seen to vary by a factor of ~3 with channels 1 and 8 having lower gain. Based on a broader set of calibration data than can be shown here, a possible cause of this variation is the influence of stray vertical magnetic field which is proportional to the plasma current (1.7 MA in this case). At lower plasma current, experiments show that the sensitivity of the NPA channels is more uniform. This effect tends to be minimized by operating the phototubes at the highest bias consistent with remaining below output signal saturation. Consequently, the NPA detectors require renormalization of the channels for the specific plasma current and phototube bias under which the measurements were obtained.

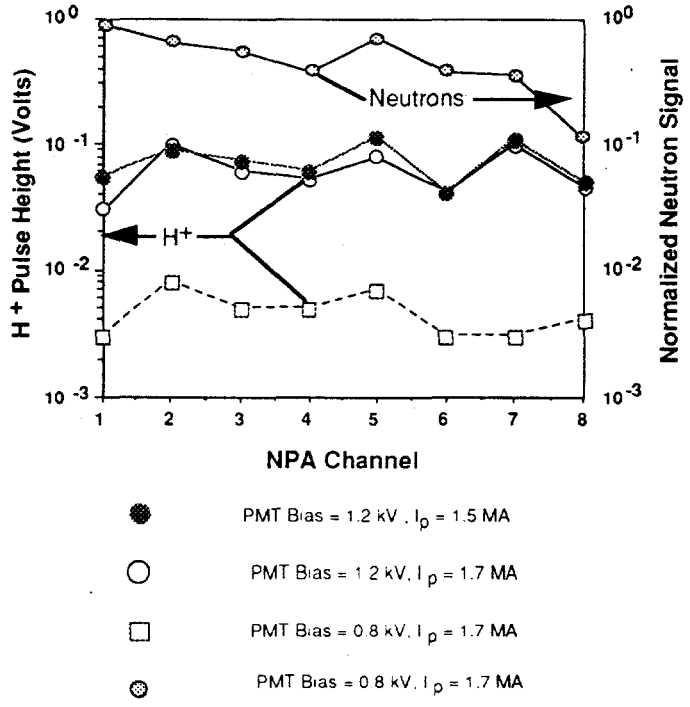

Fig. 11 H^+ pulse height distribution for all NPA channels with phototube biases of voltages of 0.8 kV and 1.2 kV. The data for the solid and open circles were obtained about a year apart and illustrate the stability of the channel normalization with time. The dotted circles illustrate the channel normalization obtained by measuring the pulse height distribution of signals induced by D-D neutrons. This data represents the ratio of the neutron pulse height to the pulse height for a single H^+ pulse for an energy of 1 MeV, both taken at the same phototube bias.

The average pulse height normalized to the energy of H^+ ions for each of the eight NPA channels discussed above was used to generate the *relative* normalization factors for the NPA channels as listed in Table II.

Table II
Relative Normalization of the NPA Channels

NPA Channel, n	Relative Normalization, ζ_n
1	0.38
2	1.00
3	0.62
4	0.53
5	0.80
6	0.41
7	1.00
8	0.46

Some further characteristics of the channel normalization are illustrated in Fig. 11. The solid circles show normalization data for a phototube bias of 1.2 kV obtained under essentially the same conditions, but taken approximately one year apart This result demonstrates that the long-term stability of the detector normalization is satisfactory. The lower curve shows the effect of reducing the phototue bias to 0.8 kV. The "neutron" data shown in the upper curve are discussed in Sec. 3.3.

It is clear that the variation in channel sensitivity has to be taken into account in deducing the energy spectra of the particles measured by the NPA. The normalization procedure described above also provides information on the absolute amplitude of single pulses of the detected particles, which allows the number of particles detected by the NPA channels in current (analog) mode to be estimated.

The neutron flux produced in D-D and D-T discharges generates a background signal in the NPA detectors. While this background is undesirable, it can be exploited to measure the gain characteristics of the phototubes for the various NPA channels. Fig. 12 presents the normalized neutron signal in D-T discharges versus the phototube

bias for channels 1 to 4. This plot shows the dependence of phototube gain, G, on the bias voltage, V. This dependence can be expressed as $G = k\,V^{\gamma}$ where γ is in the range of 5.7 - 6.3 for the different channels. The same dependence was observed in the variation of the H^+ pulse height as a function of phototube bias. This expression was used for comparison of the NPA signals detected with different phototube biases. An important point to note is that the dependence of the phototube gain on bias does not vary with plasma discharge current, which means that even under the residual influence of the stray magnetic field the phototubes are still operating in a linear regime.

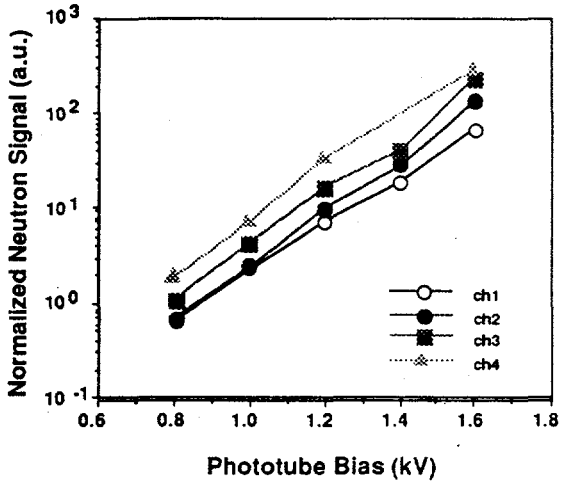

Fig. 12 Typical gain characteristics of NPA photomultiplier tubes obtained using the neutron-induced background signal

The above procedure for checking the NPA channels using H^+ and neutron signals was repeated periodically to monitor the accuracy of the NPA calibration data.

3.3 Neutron and Gamma-ray Induced Background

The radiation background is produced mainly by Compton electrons generated by gamma-ray interactions in the scintillator, the window glass and phototube as well as by energetic protons and alphas born in (n, p) and (n, α) reactions in the scintillator and nearby materials. Calculation of the D-T neutron flux, Φ_n, at the location of the NPA detectors in the absence of radiation shielding shows that $\Phi_n \sim 10^{-8}\, S_N\, cm^{-2}s^{-1}$ where S_N is total neutron yield. With the radiation shield installed, the neutron flux at the scintillator is given by $\Phi_n^* = 10^{-8}\, S_N\, \eta$ where η is the shield attenuation. Using the measured attenuation of $\eta = 1/100$ for D-T plasmas, we get $\Phi_n^* = 1.0 \times 10^8\ cm^{-2}s^{-1}$ for a typical D-T shot ($S_N = 10^{18}\ s^{-1}$). In Fig. 11, radiation induced background signals (hatched circles marked 'neutrons') corresponding to a D-T neutron yield of 10^{18} n/s are compared with the pulse height of single H^+ particles for all NPA channels with the same phototube bias of 0.8 kV. In this case, the signal-to-noise ratio for single particle detection is equal to $\sim 10^{-2}$. In the TFTR D-T experiments, pellets for PCX diagnostic measurements typically are injected 0.2 to 0.5 s after termination of neutral beam heating. This timing delay leads to deeper penetration of the pellet into the plasma as

well as to enhancement of the signal-to-noise ratio because the radiation background decays at least by a factor of 10 at this time. Under these conditions, single alpha-particle pulses can be detected by the PCX diagnostic even for high fusion power D-T shots ($S_N = 2 - 3 \times 10^{18}\ s^{-1}$).

4. Neutralization Effects in Pellet Ablation Clouds

The Pellet Charge Exchange technique is based on neutralization of the energetic ions of interest in the plasma ablation cloud surrounding an injected impurity pellet. For PCX measurements, lithium pellets are of special interest because they are used for wall conditioning on TFTR[16] and because the cross sections for neutralization of alpha particles are relatively large compared with boron or carbon. A large spatial region of the ablation cloud is expected to be dominated by the helium-like ionization state of lithium. Evidence of this is provided by Fig. 13, which shows light intensity contours of the Li^+ line radiation at 5485 ± 50 Å from a lithium pellet

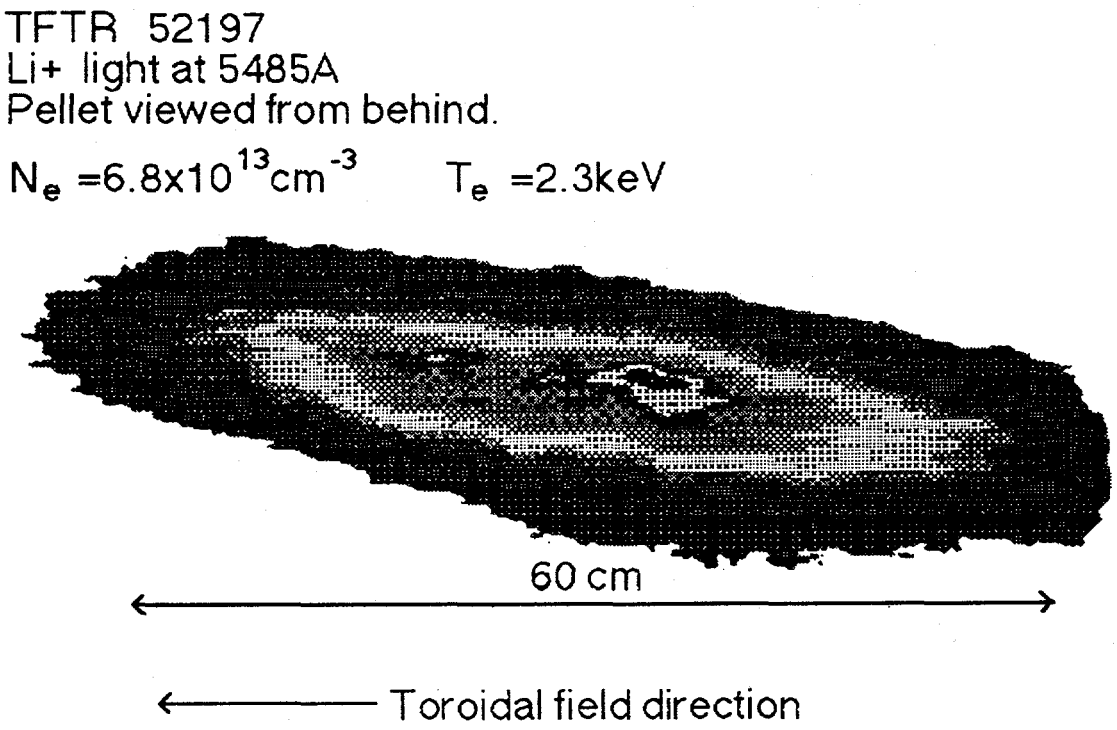

Fig. 13 Spatial contours of the lithium 5485Å line emission for lithium pellet injection in a TFTR ohmically heated plasma.

injected into an ohmically heated discharge in TFTR. As can be seen, the ablation cloud extends approximately ± 30 cm toroidally on each side of the pellet[4]. Boron pellets are also of interest for PCX measurements because the higher heat of ablation energy of 5.3 eV/atom for boron compared with 1.6 eV/atom for lithium should increase the pellet penetration and consequently access a region of higher alpha density deeper in the plasma core.

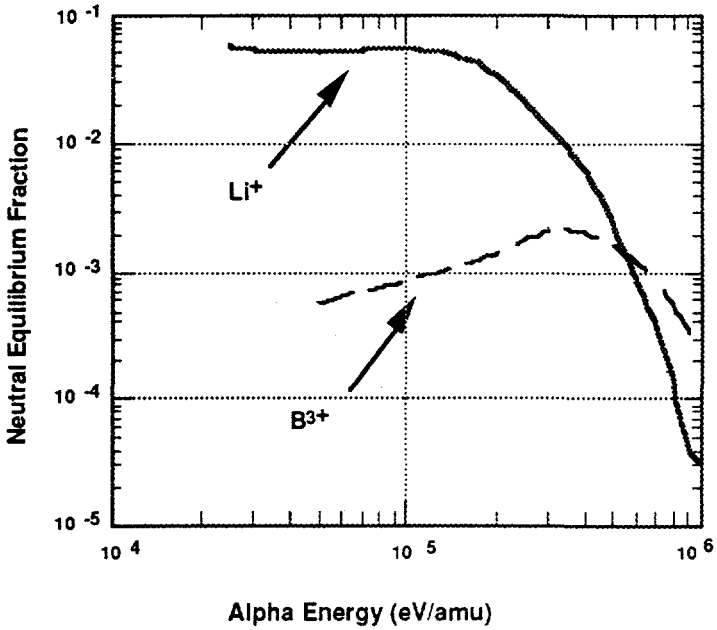

Fig. 14 Calculated neutral equilibrium fractions for α-particles on Li^+ and B^{3+} targets.

The equilibrium fraction curves for neutralization of alpha particles on a L^+ and B^{3+} targets as a function of the alpha energy, E(eV/amu), are presented in Fig. 14. Note that boron pellets have the added advantage that for alpha energies above ~ 2 MeV the calculated alpha equilibrium fraction is significantly higher than for lithium. A polynomial fit to the neutral equilibrium fraction for the Li^+ target is given by:

$$\log[F_0^{\infty}(E,\alpha)_{L+}] = -6.77487 \times 10^3 + 3.05103 \times 10^3 \log E - 5.45174 \times 10^2 (\log E)^2 + 4.82719 \times 10^1 (\log E)^3 - 2.11663 (\log E)^4 + 3.67357 \times 10^{-2} (\log E)^5 \quad (5)$$

and for the B^{+3} target by

$$\log[F_0^{\infty}(E,\alpha)_{B+3}] = -7.83432 \times 10^4 + 3.19325 \times 10^4 \log E - 5.19302 \times 10^3 (\log E)^2 + 4.21095 \times 10^2 (\log E)^3 - 1.70240 \times 10^1 (\log E)^4 + 2.74476 \times 10^{-1} (\log E)^5. \quad (6)$$

In general, the neutralization process can be a complicated function of not only the ablation cloud parameters but particle orbit effects as well. Interpretation of the PCX measurements is straight forward only if the line integral cloud density is

sufficiently high so that the charge changing reactions are independent of the density and attain an equilibrium fraction, but not so high that scattering and energy losses in the cloud need to be considered. Initially, the interaction of alphas with the pellet cloud was examined using an analytical single pass equilibrium fraction model. Recently, a more detailed Monte Carlo numerical analysis[13] which examined the effects of cloud shape, ion density and charge state composition as well multiple passes through the cloud due to the finite alpha Larmor orbit concluded that:

- For the estimated ablation cloud densities ranging from 5 x 10^{15} cm^{-3} to 1 x 10^{17} cm^{-3} in TFTR, the alpha particles reach an equilibrium fraction in the target cloud.
- Scattering and energy loss were unimportant for alpha energies above ~ 0.5 MeV.
- Inclusion of multiple passes of the alpha particles through the ablation cloud due to their finite Larmor orbit has a negligible affect the energy dependence of the alpha spectrum for energies above ~ 1 MeV, but does cause a modest reduction in the alpha flux to the analyzer.
- The mixture of ionization states of lithium in the ablation cloud affects the signal level for the PCX diagnostic, but does not significantly affect the energy dependence of the neutral equilibrium fraction as shown by the computed cases in Fig. 15. Hence the PCX measurements are insensitive to the unknown cloud charge composition, and the energy spectra can still be readily unfolded from the data.

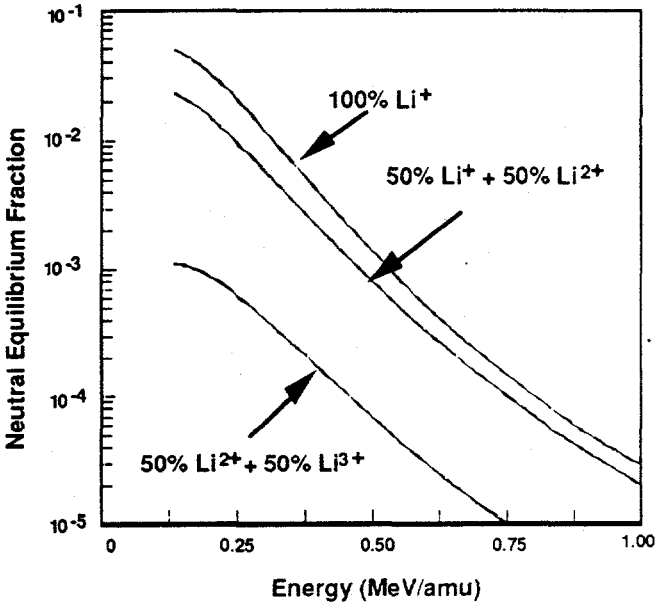

Fig. 15 Illustration of the effect of lithium ionization state mix on the computed neutral equilibrium fractions for alpha particles .

In summary, the details of the pellet ablation cloud characteristics and alpha orbits collectively have little effect on the energy distribution of the neutral flux seen by the analyzer. However, these factors do make the absolute alpha density measurements difficult.

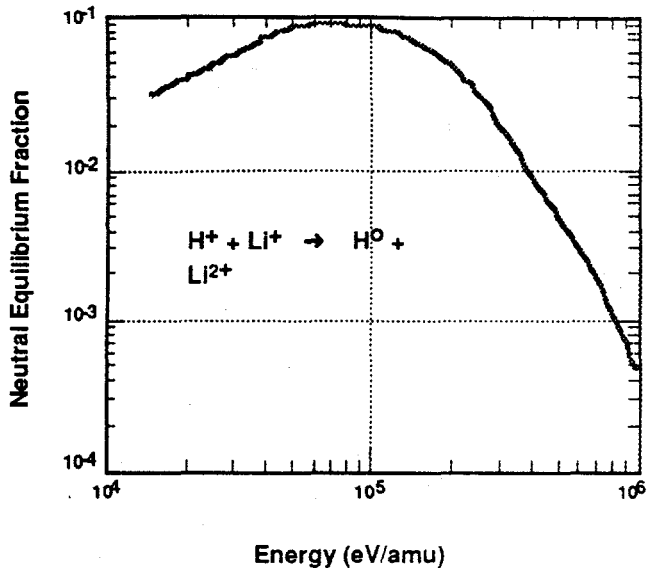

Fig. 16 Computed equilibrium fractions for H^+ (or D^+, T^+) ions on a L^+ target.

The PCX diagnostic is also used to obtain active measurements of the energy spectra of tritons from D-D reactions and the energetic ion tail distributions resulting from RF-driven hydrogenic minorities. The equilibrium fraction, $F_0^\infty(E, A^+)$, for $A^+ = H^+$, D^+ or T^+ on a Li^+ target is shown in Fig. 16.

A polynomial fit to this equilibrium fraction curve as a function of the particle energy normalized to the atomic mass, E(eV/amu), is given by:

$$\log[F_0^\infty(E, A^+)_{L+}] = 7.81374 \times 10^2 - 2.80338 \times 10^2 \log E + 3.68501 \times 10^1 (\log E)^2 - 2.10758 (\log E)^3 + 4.41404 \times 10^{-2} (\log E)^4. \quad (7)$$

5. IPI Operation and Impurity Pellet Behavior.

The Impurity Pellet Injector(IPI) used in conjunction with the PCX diagnostic is capable of injecting Li, B and C pellets with either hydrogen or helium as the gas propellant. For PCX diagnostic purposes, two pellets can be injected into a discharge with a minimum temporal spacing of 2 ms. For most experiments, cylindrical Li pellets of 2.0 mm diameter by ~ 2.0 mm length containing ~ 10^{20} atoms were inject with velocities in the range of 400 - 600 m/s. In the TFTR D-T experiments, pellets typically are injected 0.2 to 0.5 sec after termination of neutral beam heating. This timing delay leads to deeper penetration of the pellet as a result of decay of the plasma electron temperature as well as to enhanced signal-to-noise ratios because the neutron and gamma-ray induced background decays significantly faster than the confined alpha population.

The key to a successful PCX measurement is good pellet penetration. We empirically observe a degradation in pellet penetration at higher plasma electron temperature, as shown in Fig. 17. In this figure, the electron temperature and the

associated electron density for the same discharge are core values measured at pellet injection time, which was 100 ms after termination of neutral beam injection.

Several schemes were implemented to enhance the pellet penetration. One of the most effective methods is to increase the pellet velocity by replacing the helium

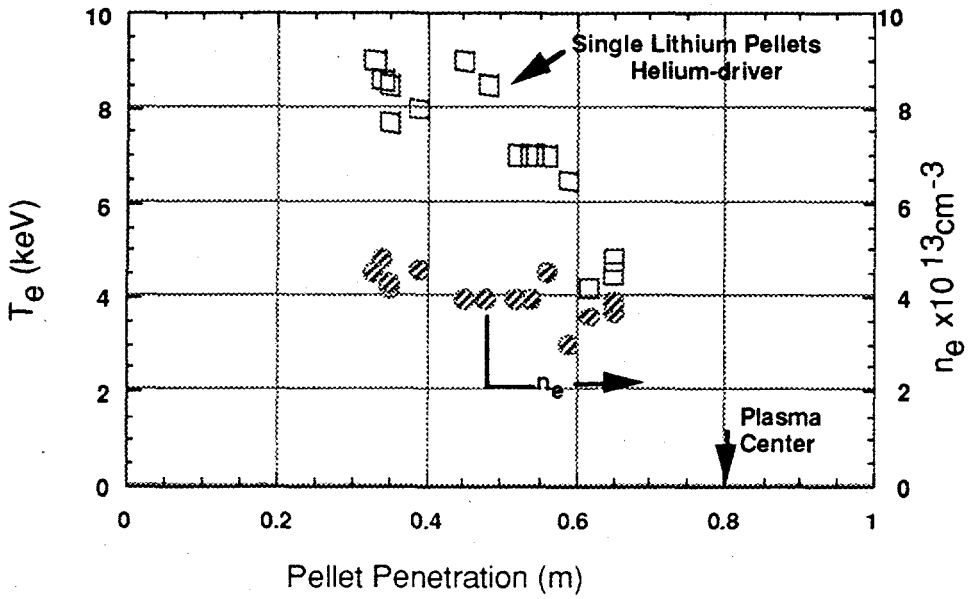

Fig. 17 Measured litium pellet penetration as as function of the central electron temperature and density at the time of pellet injection. In all cases, a single He-driven Li pellet was injected at 100 ms after termination of neutral beam heating in the plasma with R_{maj} = 2.52 m and a = 0.8 m.

gas propellant with hydrogen. With hydrogen, the measured pellet velocity increased from 500 m/s to 600 m/s and the pellet penetration increased by 10-20 cm. In addition, pellet penetration was observed to be increased by utilization of larger pellets. The influence of pellet size on penetration was examined by varying the length of the pellet by ±25% around the median value of 2.0 mm.

We also investigated the use of boron pellets as a way to improve pellet penetration. The higher heat of ablation energy for boron compared with lithium should increase the pellet penetration. In practice, this gain is offset by a lower pellet velocity from the injector due to the larger mass of boron relative to lithium. Nevertheless, an increased penetration for boron pellets ranging up to 20% (~ 12 cm) relative to lithium pellets of comparable mass is observed experimentally. PCX measurements of alpha energy spectra using boron pellets agree with lithium results and boron pellets allow the alpha energy spectrum to be measured up to 3.5 MeV [9].

The agreement of the alpha energy spectra measured with boron and lithium pellets despite the very different energy dependencies of their respective equilibrium fractions adds confidence to the neutralization fraction models used in the PCX diagnostic.

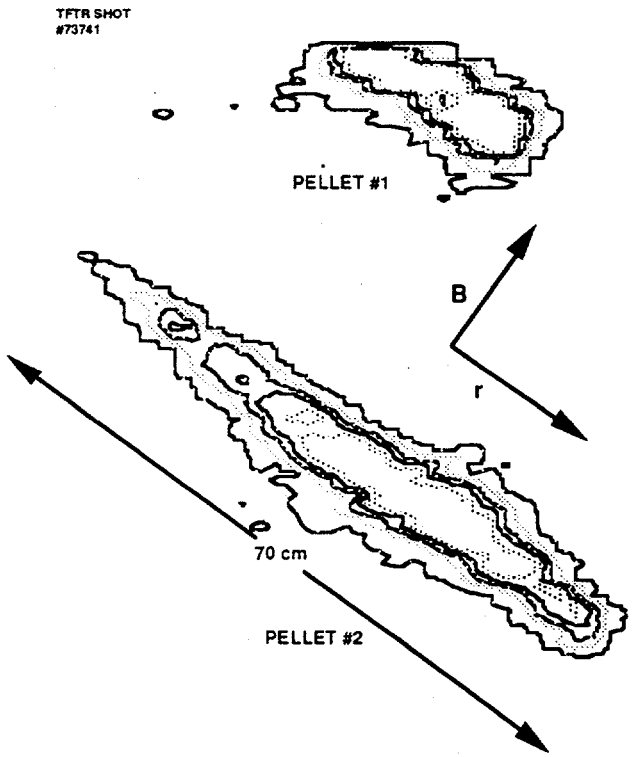

Fig. 18 CCD images illustrating the improved pellet penetration observed using "stacked pellets" in a plasma with 4.2 MW of ^3He RF minority heating. The first pellet penetrated weakly and was deflected while the second pellet penetrated ~ 70 cm without significant deflection.

Another method for improving pellet penetration is to use two "stacked" pellets: i.e. firing two pellets with a short time delay between the first and second pellets. While the first pellet penetrates poorly, it lowers the plasma temperature to allow the second pellet to penetrate farther. The stacked behavior was verified experimentally in an RF-only heated discharge (# 73741, R = 2.62 m, a = 0.96 m) with double Li pellet injection (τ_{sep} ~ 20 ms) where the two pellets were injected at the end of a 4.3 MW RF pulse. A CCD camera located at the bottom of the vessel was used to produce a snapshot of the ablation clouds for this case, as illustrated in Fig. 18. The first pellet penetrated ~ 65 cm to r/a ~ 0.68 and was slightly deflected out of the NPA sightline, but it opened a path for the second pellet which was not deflected and penetrated an additional 30 cm to the plasma core. As illustrated by the $^3He^{++}$ measurements

shown in Fig. 19, the PCX signals in this discharge are much stronger for the second pellet compared with the first. The stacked pellet scenario works very well in RF discharges[6] and in post-NBI discharges [10].

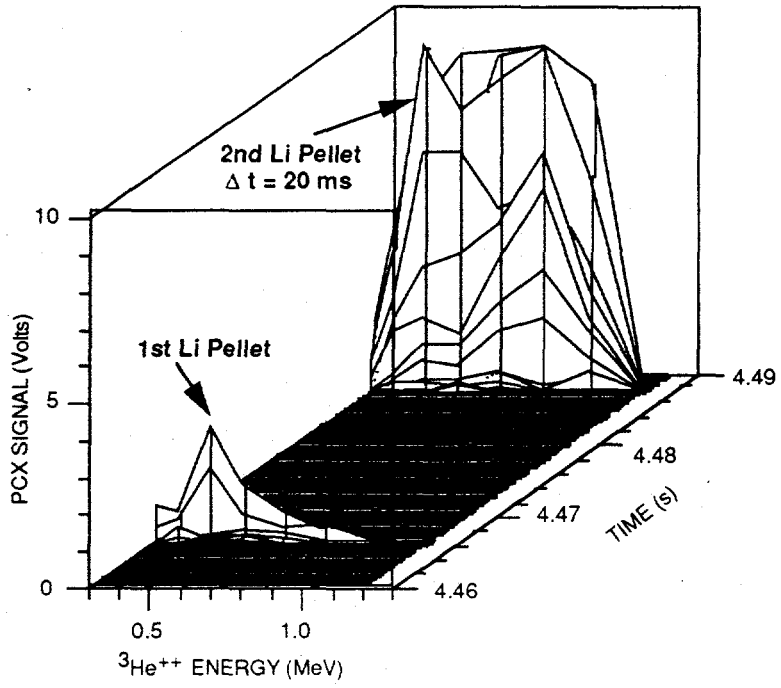

Fig. 19 Illustration of the enhanced PCX $^3He^{++}$ signal for the second pellet using "stacked" lithium pellet injection (same TFTR discharge as in Fig. 18).

A concern with stacked pellets is that the first pellet might perturb the measurement by the second pellet. Hence, the time delay between successive pellets, τ_{sep}, must be kept short compared to the time scale, τ_{sl}, for slowing down of the particle being measured. Under experimental conditions typical of PCX operation, τ_{sep} ~ 5 - 20 ms and $\tau_{sep} << \tau_{sl}$, where the slowing down time, τ_{sl}, is in the range of 200 - 500 ms for light ions in the MeV energy range. Evidence corroborating this behavior is provided by the example in Fig. 20, which shows that the alpha density profiles obtained from the first and second pellets largely coincide to within the error bars of the data points.

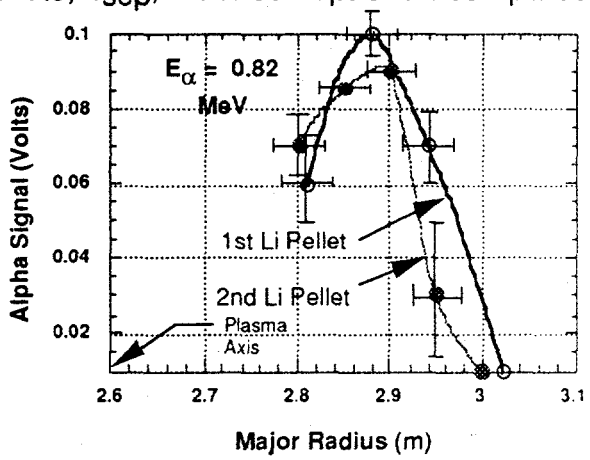

Fig. 20 Example of alpha density profile measurements using stacked pellets.

This data was acquired after a sawtooth crash which lowered the plasma electron temperature enough to allow reasonable penetration for the first pellet. On occasion, however, the first pellet does perturb the measurement by the second pellet. But when this occurs, the irregularity in the data is very obvious; for example, the energy spectrum for the second pellet will be "cold" relative to that from the first pellet. The reason for this occasional irregular behavior is not understood at this time.

6. PCX Operation and Data Analysis

In this section, a brief description of the data analysis procedure and the numerical codes used to model the PCX measurements is presented, followed by data sets which illustrate the operation of the diagnostic.

The alpha energy distribution in the plasma in the direction of observation, dn_α/dE (a.u.), is derived from the measured PCX signals, Γ_n (volts), using the following expression:

$$dn_\alpha/dE \propto K(E)\,\Gamma_n \tag{8}$$

where

$$K(E) = \left\{ F_0^\infty(E)\, v_\alpha\, A_{cloud}\, \frac{\Omega}{4\pi}\, \eta_n(E)\, (\Delta E_n/E_n)\, E_n\, \zeta_n \right\}^{-1} \tag{9}$$

and

$F_0^\infty(E)$ = neutral equilibrium fraction,

v_α = ion velocity associated with energy E,

A_{cloud} = area of the portion of the ablation cloud observed by the NPA,

$\frac{\Omega}{4\pi}$ = solid angle of the analyzer,

$\eta_n(E)$ = calibrated analyzer detection efficiency,

$\Delta E_n/E_n$ = energy resolution of the analyzer (see Table I),

E_n = energy of the n^{th} NPA channel, and

ζ_n = relative normalization of the NPA channels (see Table II).

Note that K(E) must be evaluated for the individual NPA channels. The value of $F_0^{\infty}(E)$ is obtained from modeling calculations[8,13]. The relative normalization factor, ζ_n, was discussed in Sec. 3.2. The energy spectra of other ion species is obtained by using the values of $F_0^{\infty}(E)$, v_α and $\eta_n(E)$ appropriate to that species.

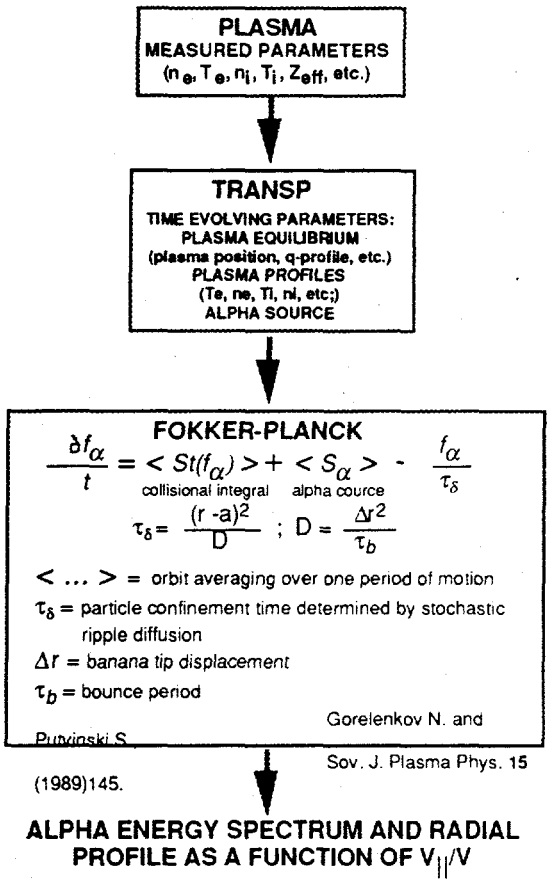

Fig. 21 Flow diagram illustrating the codes used to model the PCX data.

During the analysis of first PCX experimental results, we found that three factors can have a significant influence on interpretation of the measurements. These are: 1) the classical slowing down process, 2) toroidal magnetic field ripple, and 3) sawtooth oscillations which usually occur after termination of neutral beam injection. In analyzing the PCX data, we have attempted to take these effects into account by using two numerical modeling codes. A flow diagram of the codes is shown in Fig. 21. First of all, we used the TRANSP[18] Monte-Carlo Code which follows the orbits of alphas as they slow down and pitch angle scatter by Coulomb collisions with the background plasma. TRANSP assumes that the alphas are well confined during the slowing down and takes into account the spatial and temporal distributions of plasma parameters for each particular shot. TRANSP was recently modified to include the stochastic ripple diffusion of alphas[19]. To model ripple effects for analysis of the PCX measurements, it is necessary to constrain integration of the alpha pitch angle to a narrow range around the PCX observation angle, $V_{||}/V = -0.048$, because of the significant dependence on pitch angle of the alpha confinement time in the presence of stochastic ripple diffusion. Since the Monte-Carlo methods used in TRANSP are computationally intensive, we developed a fast Fokker-Planck Post TRANSP (FPPT) processor code based on a numerical solution of the drift-averaged Fokker-Planck equation. FPPT uses the pitch

angle integrated alpha source distribution provided by TRANSP and calculates radially resolved alpha energy spectra for the specific pitch angle viewed by the PCX diagnostic. This code includes ripple effects, but the collisional integral used in the Fokker-Planck equation does not include pitch angle scattering or velocity diffusion. The TRANSP and FPPT calculations agree well when the modeling basis for both codes are applicable.

A model for mixing of trapped particles has been implemented in the FPPT code to compute the density profile broadening of energetic ions due to strong sawtooth activity[20]. The model includes both conventional "magnetic mixing" which affects primarily passing particles as well as a novel "electric field mixing" which affects primarily trapped particles. The later model is based on the non-resonant effect of confinement of trapped particles inside a potential well with an adjustable characteristic perpendicular electric field. Due to assumed breakdown of toroidal symmetry at the sawtooth crash, fast particle drift in the electromagnetic field may lead to radial diffusion of trapped alpha particles.

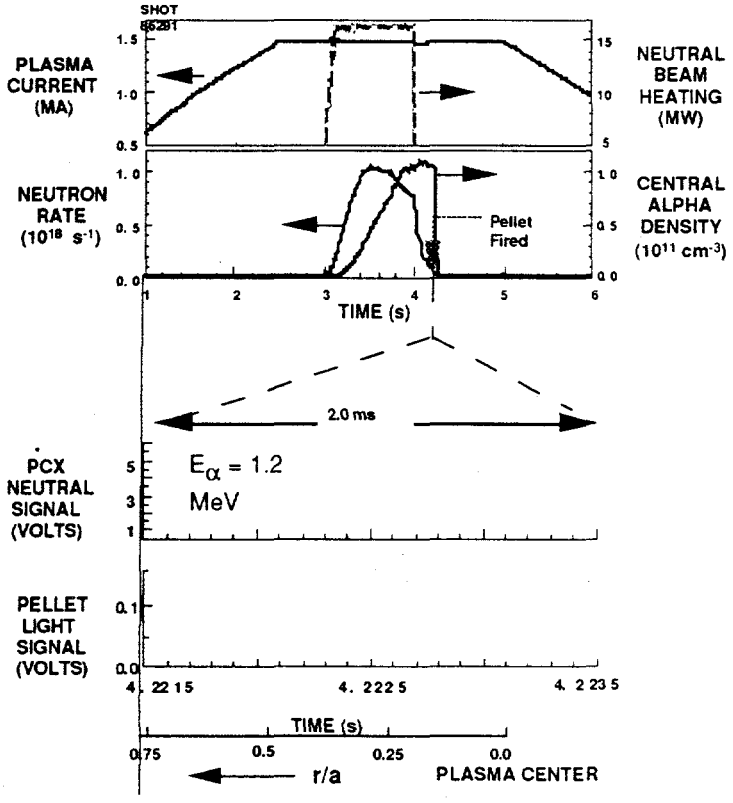

Fig. 22 Selected plasma waveforms and PCX signals for measurement of the alpha spectrum up to the birth energy using single B pellet

In order to separate the classical behavior of alpha particles from the other effects which were discussed above, measurements of the alpha energy spectra were obtained in core of quiescent D-T plasmas in TFTR. Selected plasma waveforms and pellet charge exchange signals for these measurements are presented in Fig. 22. All waveforms are diagnostic measurements except for the central alpha density, which is a TRANSP calculation. The basic discharge parameters were: R_{maj} = 2.52 m, a = 0.8 m, I_p = 1.5 MA, and B_T = 5.2 T. A typical PCX signal along with the pellet light emission is shown at the bottom of

Fig. 22. The light emission from the pellet ablation cloud represents the charge exchange target provided by the pellet, which typically burns out in < 2 ms. The pellets are injected perpendicularly into the plasma at the midplane. Hence the time evolution of the signals also reflect their variation with radial position inside the plasma. A key feature of all the PCX alpha signals is the delay in their rise relative to the light emission signal. In other words, we observe no alpha signal until the pellet penetrates to a certain plasma radius. The depleted region of the signal is observed in all discharges with PCX data and is attributed to stochastic ripple diffusion[12].

The fluctuation in the PCX signals evident in Fig. 22 are observed in most discharges. Although signal statistics could well be a contributing factor, these fluctuations could be a real effect of pellet ablation behavior. Similar fluctuations have been observed in the light emission from pellet ablation clouds on other tokamaks. Several theories have been proposed to explain such fluctuations. One theory suggests that the fluctuations are due to a Raleigh-Taylor cloud instability[17]. The instability displaces the ablation cloud from the field line with the pellet, allowing the cloud to quickly become more highly ionized and resulting in a reduction in the fraction of incident alphas neutralized in the cloud. The instability essentially reduces the neutral signal until the pellet cloud is reformed by new ablation and the signal recovers. This process can occur multiple times during the pellet life time.

The alpha energy spectrum obtained from the PCX measurements for this discharge is shown by the solid circles in Fig. 23. In this "slowing down" case, (#86291, P_b = 15 MW), the alpha distribution from 1 - 3.5 MeV was obtained using a single boron pellet injected 200 ms after termination of a 1.0 s beam pulse. Note in Fig. 22 that at the selected time of pellet injection, the D-T neutron yield which gives rise to PCX signal interference has decayed significantly while the alpha density has not. Also shown (solid squares) is the energy spectrum measured for a "beam blip" case (#86299, P_b = 20 MW), where the boron pellet was injected 20 ms after a beam pulse of only 100 ms duration. Since the alphas are all created in a time interval short compared to the alpha slowing-down time (~ 500 ms), the measured energy spectrum for this short pulse neutral beam injection or "beam blip" discharge yields information on the alpha birth energy distribution. Reasonable agreement is seen between the data and the FPPT-computed slowing down curves corresponding to the PCX stochastic ripple loss boundary, which is demarcated by the hatched region. In both measurement times. The FPPT code includes Doppler broadening of the alpha particle birth energy, E_α, for which the full width at half maximum is given approximately by $\Delta E(keV) = 182(T_{eff})^{0.5}$ where T_{eff} = 30 keV is the effective

temperature of the deuterium and tritium ions.

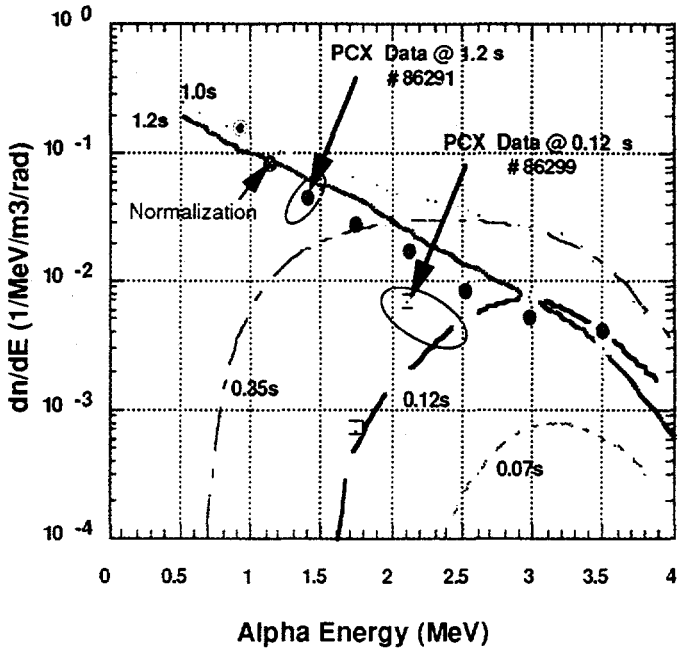

Fig. 23 Evolution of the alpha energy spectra computed using the FPPT code (curves) and comparison with the measured alpha spectra for two times: 1) near the birth phase shown as solid squares corresponding to 0.12 s and, 2) during the slowing down phase shown as solid circles corresponding to 1.2 s.

To study the influence of stochastic ripple diffusion and sawtooth oscillations on the alpha distribution, PCX data were obtained in both sawtooth free and sawtoothing D-T plasmas. The discharge conditions were: I_p = 2 MA, R_{maj} = 2.52 m, and B_T = 5 T with 20 MW of DT neutral beam power injection for 1.1 s. For high power neutral beam heated discharges in TFTR, the sawtooth oscillations usually begin around 0.2 - 0.3 s after termination of neutral beam heating. The PCX data before a sawtooth crash was obtained on discharge #84550 by injecting two Li pellets 0.3 s after beam termination with a 10 ms interval between them (stacked pellets). To obtain PCX data following the first sawtooth crash, two stacked pellets were injected 0.4 s after termination of neutral beam heating in discharge #84549 which had similar parameters the sawtooth free condition.

Shown in the upper panel of Fig. 24 are the measured alpha energy spectra in the plasma core for the sawtooth free case and at R_{maj} = 2.9 m for the sawtoothing case showing that the energy spectrum steepens after the crash. Shown in the lower panel are the alpha density radial profiles for an alpha energy of 1.21 MeV plotted as a

function of the plasma major radius for both the sawtooth free and sawtoothing discharges. It is clear that large sawteeth cause broadening of the alpha density profile to well outside of the q = 1 radius. The radial redistribution is bounded by the panels, the discrete points correspond to the various energy channels of the NPA while the curves correspond to the FPPT calculations. The error bars shown reflect the statistical errors due to the counting statistics and the radial resolution of the PCX system. Note that the normalization of the PCX and modeling data was made only once for the sawtooth free energy spectrum and then used in the other cases. The data for the sawtooth free case were derived from the second of two stacked pellets

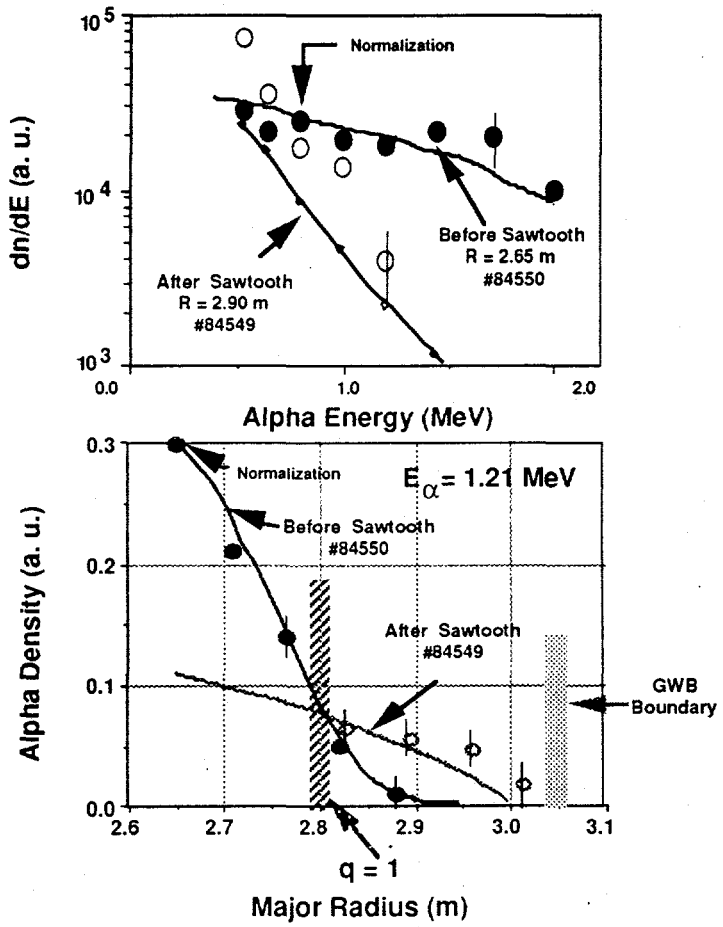

Fig. 24 PCX alpha energy spectra (upper panel) at two major radii and alpha density radial profiles at an alpha energy of 1.21 MeV (lower panel) for sawtooth free and sawtoothing discharges together with the modeling results from the FPPT code. For the deeply trapped alpha particles which the PCX diagnostic measures, large sawteeth produce a strong depletion of the alpha core density and a significant broadening of the density profile well beyond the q = 1 surface. The magnitude of this mixing is observed to decrease with increasing alpha energy.

while the data for sawtoothing case correspond to the first pellet.

To summarize the results in Figs. 23 and 24, we conclude that in the TFTR plasma core under sawtooth free conditions, trapped alpha particles are well confined and slow down classically. In more radially outboard plasma regions, the trapped alphas begin to be affected by stochastic ripple diffusion. Post neutral beam injection sawtooth oscillations in TFTR effectively transport fast trapped alphas radially outwards with the extent bounded by the stochastic ripple loss region. This transport can lead to enhanced first orbit and ripple losses of trapped fast alphas, which potentially could damage the first wall of high fusion power tokamaks including ITER.

Future Work

As described in this paper, the Pellet Charge Exchange diagnostic on TFTR has been used primarily to obtain active charge exchange measurements in conjunction with impurity pellet injection with the detector system operated in the current mode. While passive measurements in the pulse counting mode have also been obtained, operation in this mode is very restrictive with pulse counting rates limited to less than ~ 10 kHz in the absence of any significant neutron and gamma induced background signal. Efforts are in progress to upgrade the pulse counting capability by implementing a detector system developed by the Ioffe Institute and previously operated on JET and JT-60U[21]. This system consists of CsI(Tl) scintillators with features designed to minimize signals induced by background neutron and gamma rays and is equipped with 16-channel pulse height analysis electronics on each of the eight NPA energy channels. Provision will be made to remotely select either the current or the pulse counting modes. After commissioning near the end of the present calendar year, we will examine passive measurements, for example, of alpha particles which are neutralized by charge exchange on the helium-like ionization state of the intrinsic carbon impurities in TFTR and of hydrogenic ions (e.g. H^+ and tritons) neutralized on hydrogen-like carbon.

Acknowledgments

This work was supported by US DoE Contract DE-AC02-76-CHO-3073 and US DoE Grant DE-FG03-92ER54150.

References

1 G. McKee, R. J. Fonck, B. C. Stratton, *et al.*, Phys. Rev. Lett. **75**, 649 (1995).

2 P. P. Woskov, J. S. Machuzak, R. C. Myer, *et al.*, Rev. Sci. Instrum. **59**, 1565 (1988).

3 R. K. Fisher, J. S. Leffler, A. W. Howald, *et al.*, Fusion Technol. **13**, 536 (1988).

4 R. K. Fisher, J. M. McChesney, A. W. Howald, *et al.*, Rev. Sci. Instrum. **63**, 4499 (1992).

5 S. S. Medley, R. K. Fisher, A. V. Khudoleev, *et al.*, Proceedings of the 20th European Physical Society Conference on Controlled Fusion and Plasma Physics, (Lisbon, Portugal, July 1993), Vol. <III>, 1183-1186.

6 J. M. McChesney, H. H. Duong, R. K. Fisher, *et al.*, Rev. Sci. Instrum. **66**, 348 (1995).

7 R. Majeski, J. H. Rogers, S. H. Batha, *et al.*, "ICRF Experiments in TFTR with Fast Waves and Mode Converted Ion Bernstein Waves, " Accepted for publication in Physics of Plasmas (May, 1996).

8 R. K. Fisher, J. M. McChesney, P. B. Parks, *et al.*, Phys. Rev. Lett. **75**, 846 (1995).

9 S. S. Medley, R. V. Budny, D. K. Mansfield, *et al.*, Proceedings of the 22nd European Physical Society Conference on Controlled Fusion and Plasma Physics, (Bournemouth, United Kingdom, 3-7 July 1995), Vol. **19C**, I-409.

10 M. P. Petrov, R. V. Budny, H. H. Duong, *et al.*, "Studies of Energetic Confined Alphas Using the Pellet Charge Exchange Diagnostic on TFTR," Nuc. Fusion **35**, 1437-1443 (1995).

11 D. W. Johnson, V. Arunasalam, C. W. Barnes, *et al.*, "Recent D-T Results on TFTR," Plasma Phys. and Control. Fusion **37**, A69-A85 (1995).

12 H. H. Duong, R. K. Fisher, S. S. Medley, *et al.* ,"The effects of Toroidal Field Ripple on Confined Alpha Measurements in TFTR D-T Plasmas," PPPL-3178, (March, 1996) 26 pp. Submitted to Nucl. Fusion (February, 1996).

13 J. M. McChesney, P. B. Parks, R. K. Fisher and R. E. Olson, "The Interaction of Fast Alpha Particles with Pellet Ablation Clouds," General Atomics Report, GA-A21958 (December, 1995).

14 A. B. Izvozchikov, A. V. Khudoleev, M. P. Petrov, *et al.*, JET Joint Undertaking, Abingdon, Oxfordshire, England, Report JET-R(91) 12, (1991).

15 M. P. Petrov, V. I. Afanasiev, S. Corti, *et al.*, Proceedings of the 19th EPS Conference on Controlled Fusion and Plasma Physics (Innsbruck, 1992) I-1031.

16 D. K. Mansfield, J. D. Strachan, M. G. Bell *et al.*, "Enhanced Performance of Deuterium-Tritium Fueled Supershots using Extensive Lithium Conditioning in the Tokamak Fusion Test Reactor," Phys. Plasmas **2**, 4252-4256 (November, 1995).

17 P. B. Parks "Theory of Pellet Cloud Oscillation Striations," Rep. No. GA-A22005, General Atomics, CA (1995), Plasma Phys. and Control. Fusion **38**, 1-21 (1996).

18 R. V. Budny, M. G. Bell, A. C. Janos, *et al.*, Nuclear Fusion **35**, 1497 (1995)

19 M. H. Redi, R. V. Budny, D. S. Darrow, *et al.*, "Modeling of TF Ripple Loss of Alpha Particles in TFTR DT Experiments," PPPL-3113 (July 1995) 28 pp. Nucl. Fusion **35**, 1509-1516(1995).

20 N. N. Gorelenkov, R. V. Budny, H. H. Duong, R. K. Fisher, S. S. Medley, and M. P. Petrov, "Modeling of α-Particle Redistribution by Sawteeth in TFTR," PPPL-3184 (April, 1996) 17 pp. To be submitted to Nuclear Fusion.

21 V. I. Afanassiev, Y. Kusama, M. Nemoto, *et al.*, Proceedings of the 22nd European Physical Society Conference on Controlled Fusion and Plasma Physics, (Bournemouth, United Kingdom, 3-7 July 1995), Vol. **19C**, II-057.